Local dynamics of pharmaceutical powder fluidization using high speed long distance microscopy and particle image velocimetry

Elserfy, K.[1], Cheng, S.[1,*], Chan, H-K.[2], and Kourmatzis, A.[3]

1-School of Engineering, Macquarie University, NSW 2109, Australia

2-Advanced Drug Delivery Group, School of Pharmacy, University of Sydney, NSW 2006, Australia

3-School of Aerospace, Mechanical and Mechatronic Engineering, University of Sydney, NSW 2006, Australia

*shaokoon.cheng@mq.edu.au

Abstract

The local dynamics of fluidized pharmaceutical carrier powders in a turbulent channel flow was studied using particle image velocimetry (PIV) and High-speed, long-distance microscopy (HS-LDM). Four different lactose powders which have been used as a drug carrier in dry powder inhalers were used in this study. These powders have median powder particle diameters ranging between 61 and 121 μm. Air flow velocities ranging between 13.3 m/s and 66.7 m/s were examined. In addition, the effect of grid blockage ratio (ranging from ~25% to ~40% of the area of channel cross-section) was also investigated. Results show that the high-speed, long-distance microscopy (HS-LDM) technique was able to capture the mean velocity of the particles, and the results corresponded well with the PIV measurements. Results from the high-speed, long-distance microscopy (HS-LDM) method also demonstrate that the span of particle velocity closely follows that of the particle size distribution both for cohesive and non-cohesive powders. This study contributes towards an improved understanding of pharmaceutical carrier dynamics in turbulent channel flows and demonstrates how advanced image processing can be used to capture local particle dynamics.

Keywords

Two-phase flow; dry powder inhalers; Lactose carriers; pharmaceutical carriers; advanced imaging techniques

1. Introduction

Dry powder inhalers (DPI) have been widely used for the delivery of medication to treat respiratory diseases such as asthma and chronic obstructive pulmonary disease. In these devices, the dose of active pharmaceutical ingredient (API) is fluidized by exposure to an airstream induced by the patient. Carrier particles are attached to API particles to improve the flowability of powder and dispersion [1]. DPI performance has been largely known to depend on inhaler design, air flow rate generated by the patient [2-6], and powder formulation. With regards to powder formulation, the carrier particle morphology is critical. DPI behaviour can be modified by changing the carrier shape [7], altering carrier size [8], or coating particles to decrease inter-particle cohesion [9]. Increasing the in-situ generation of carrier fines using different blending methods [10] have also been demonstrated as useful means of improving DPI performance.

Many experimental studies have used particle image velocimetry (PIV) to study the performance of DPIs by investigating powder particle dynamics and powder evacuation in the devices. Han et al. [11, 12] investigated the flow field distribution and drug dispersion mechanism inside the mouthpiece of a Spiros® inhaler using PIV. It was concluded that impaction was the dominant mechanism in the tested inhaler. Kou et al. [13] used PIV to demonstrate that there were at least three dispersion mechanisms in a transparent Rotahaler® model device and they were the drag force, impact with an obstacle, and particle-particle collision. Pasquali et al. [14] investigated the fluidization of lactose powder blend in a transparent Nexthaler® using high-speed imaging and PIV. The study demonstrated that flow exiting the device was highly turbulent with a rotating flow structure that increased the probability of wall impacts which had likely promoted carrier drug deagglomeration. Nogc et al. [15] investigated the design parameters of dry powder inhaler devices (DPI) using PIV and cascade impactors and demonstrated that the hole sizes of a grid placed after the mouthpiece had negligible effects on the turbulence intensities generated.

In addition to the experimental studies conducted on commercial DPI devices, experimental research to shed light on the fundamental mechanisms that underpin powder evacuation process and powder dynamics using simplified geometries have also been performed, albeit being rarer. The use of simpler geometries is important to isolate the role of device geometry in DPIs, and to focus on the fundamental particle-turbulence interactions and their categorization using dimensionless groups. For example, Tuley et al. [16] studied the fluidization of four different lactose powders in three simple geometries to understand the effects of geometry, inhalation profile and powder type on fluidization using high-speed imaging. Versteeg et al. [17] studied powder fluidization inside a simplified geometry by using high-speed video imaging and showed that jet impaction was a dominant powder fluidization mechanism. Powder deagglomeration was studied by Voss et al. [18] using a novel

deagglomeration rig, and the study concluded that turbulence was an effective deagglomeration mechanism. Recently, Elserfy et al. [19] studied the effects of grids with different blockage ratios on the fluidization of pharmaceutical carrier powders in a horizontal channel using global-scale high-speed imaging and PIV. The study demonstrated that a grid placed upstream of the channel (before the powder bed) was able to improve the evacuation behaviour of the carrier particles at a low flow rate, resulting in less powder residue in the powder pocket.

While PIV is commonly used in powder fluidization research, it is not able to differentiate between particle size-bands, and therefore it cannot provide simultaneous measurement of particle size and velocity. This is more of an issue when the two-phase flow is comprised largely of non-spherical particles as is the case in pharmaceutical powder formulations. given that the majority of the powders used have a broad particle size distribution and typically consist of non-spherical particles with a Stokes number above unity. High-speed, Long-distance microscopy (HS-LDM) with the capability to quantitatively analyze non-spherical particle dynamics has been extensively used in the characterization of spray flames and atomization [20-22]. Such a technique has the advantage of providing information on powder particle velocities as a function of particle size, with their equivalent diameters being measured simultaneously. Such measurements are extremely useful to improve understanding of the role of carrier particles on the performance of DPIs.

The aim of this study is to investigate particle dynamics for a range of carrier powders in a simple horizontal channel flow using PIV and HS-LDM, and to compare the two methods for a range of flow conditions. The results will establish the utility and limitations of both PIV and HS-LDM in DPI flows. The HS-LDM technique is subsequently utilized to provide measurements of size conditioned velocities. These will include local fluctuating velocity values in order to quantify the size dependent dynamics of the particles as a function of the local dimensionless numbers, such as the Stokes number. Such an analysis will enable a more detailed understanding of local powder particle dynamics, which is currently severely lacking in the pharmaceutical powder dynamics literature.

2. Methodology

2.1 Channel geometry and experimental configuration

Fluidization channels with a square cross-section with side length (W) of 5 mm (5 × 5 channel) and 10 mm (10 × 10 channel) were used (see Fig 1). The channels have a powder pocket with depth (D) and width (W). While the depth of the powder pocket (D=5 mm) is the same in the two channels, the width of the pocket is equal to the channel cross-section side length (W= 5 mm for 5 × 5 channel and W = 10 mm for 10 × 10 channel). The powder pocket is located at J = 250 mm from the channel inlet so that air flow will be fully developed before

interacting with the powder. A rotameter and pressure regulator were used to control the air flow rate supply to the channel. The air flow was initiated by a 12 V solenoid valve which was triggered by the high speed-camera when it started recording. Mean velocities ranging from ~13 m/s - ~66 m/s corresponded with the typical respiratory flowrate range of 40-100 LPM were utilized in this study.

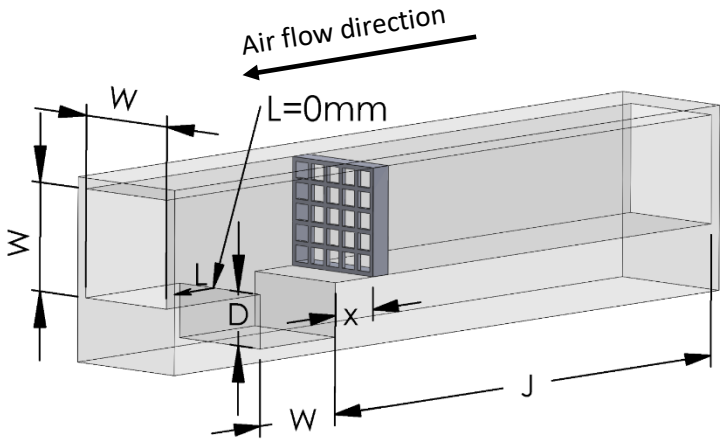

Fig. 1. Horizontal Channel layout and the dimensions of the channel, powder bed and location of the grid relative to the powder bed. D is the powder pocket depth (5 mm for both 5 × 5 and 10 × 10 channel), and W is the powder pocket width equal to the channel width (W = 5 mm for 5 × 5 channel, W=10 mm for 10 × 10 channel, J = 250 mm for both channels).

Grids were only used in the 10 × 10 channel due to limitations in manufacturing a small grid that could fit into the 5 × 5 channel. Grids with an area blockage ratio (surface area of grid normalized by the channel cross-sectional area) of ~25%, ~30%, and ~40% were used in this study. Justification for these blockage ratios and their role in the general global evacuation behaviour has been detailed in a previous study [19]. The grids were fitted into the 10 × 10 channel before the powder pocket at its edge (x = 0). The experimental configurations are summarised in Table 1 and Table 2. For the 10 × 10 channel, only air flow rates of 80 and 100 L/min were performed because powder evacuation cannot be achieved at lower flow rates for no grid cases as observed from preliminary work.

Table 1. cases studied for 5 × 5 channel

Volume flow rate (L/min)	5 × 5 channel mean velocity (m/s)	PIV	HS-LDM
40	26.7	✓	✓
60	40	✓	✓

80	53.3	✓	
100	66.7	✓	✓

Table 2. cases studied for 10 × 10 channel

Volume flow rate (L/min)	10 × 10 channel mean velocity (m/s)	Without grids		With grids	
		PIV	HS-LDM	PIV	HS-LDM
80	13.3			✓	✓
100	16.7	✓	✓		

2.2 Imaging equipment setup and image processing

2.2.1 Particle image velocimetry

For the PIV measurements (see figure 2(a)), a 300 W Oxford Lasers Firefly pulsed laser was used to produce a laser sheet at the mid-plane of the channel. Both the laser and the solenoid valve which was used to initiate the air flow were trigged by a Photron FASTCAM Mini UX100 high-speed camera. A 28 mm OZUNON camera lens with 52 mm diameter was used. An image size of 1152×158 pixels for 5× 5 channel and 835×186 pixel for 10×10 channel resulting in a spatial resolution of ~32 μm and ~54 μm respectively. Cross-correlation PIV post-processing code PIVLAB [23] was used to generate the particle velocity vectors. The PIV code employs a fast Fourier transform (FFT) window deformation multi-pass algorithm using an interrogation window with a final size of 16 × 16 pixels with 50% window overlap for computing cross-correlation. Three passes were used in the study with a first pass window size of 64 × 64 for the 10 × 10 channel or 40 × 40 for most cases of 5 × 5 channel (smaller first pass size was chosen in the 5 × 5 channel because half of the channel height was studied due to lower particles dispersion in the upper half of the channel). Two times 3-point Gaussian fit was used to refine the location of the intensity peak of the correlation matrix. Outliers from the vector field were removed by applying a threshold for acceptable velocities using graphical selection. Calibration was performed using the known dimension of the powder pocket and channel using an image for the channel prior to the PIV experiment. For the PIV measurements, the lactose carriers were the seeding particles. The PIV measurements were tested by analyzing the mean and standard deviation of the measured velocity as a function of the number of image frames used to compute statistics as shown in Fig. A4, and Fig. A5. Also, the effect of changing the number of passes and final pass size on the mean velocities for the mean velocity field of the particles has been illustrated by using one pass (64 × 64), two passes (64 × 64, and 32×32), and three passes (64 × 64, 32 × 32, and 16 × 16) in which minimal effect has been noticed in changing the final pass size as shown in table A1, and table A2 in the appendix.

2.2.2 High-speed, Long-distance microscopy (HS-LDM)

In the high-speed, long-distance microscopy (HS-LDM) setup (See figure 2(b)), the laser was placed in line with the long-distance microscopic lens (QUESTAR QM 100). The long-distance microscopic lens was attached to the high-speed camera via a swivel coupling and was focused on the midplane of the channel. A diffuser and collimating lens were connected to the end of the laser output to remove coherence so that uniform background illumination can be produced. The flow channel was placed perpendicularly to the common axis of the laser and the camera. Depending on the air flow rate, an image size of 1280 × 1024 or 1280 × 800 pixels was used to image the powder particles resulting in a spatial resolution of 2.43 μm. Similar to the PIV setup, both the air solenoid valve and the laser were triggered by the camera. The laser operated at half of the camera's frame rate, emitting two successive pulses, hence enabling velocity measurement. The separation time between the two pulses, ranging between 5 and 16 μsec, was tuned so that powder particles between successive frames can be tracked adequately for different flow rates.

An in-house MATLAB script was developed for image processing and to analyze the particle velocities. The captured images were binarized using an adaptive threshold such that the top threshold was determined as a percentage of the average image intensity. The top threshold were 35% and 45% for the 5 × 5 channel and 10 × 10 channel respectively. These thresholds are similar to the threshold used in image binarization of polydisperse turbulent sprays, which has been previously validated against phase Doppler anemometry data [21]. Particles with a major axis larger than 300 μm were identified as either two particles connected on the image frame or as a large area formed by a powder cloud of fines, these particles were removed from the image prior to computing the size and velocity statistics (highlighted with red boxes) as shown in Fig. 3 to minimize error.

Additional lower and upper thresholds for binarization (80% and 95% of image threshold respectively) were used in the binarization of each powder particle to remove some of the defocused powder particles. The percentage of change in each powder particle area was calculated. If the percentage of area change for a given particle was higher than the predetermined criteria (25% for particles with minor and major diameter > 60μm, and 90% for smaller particles), the particle will be removed (see example bounded by yellow circles in Fig 3).

(a)

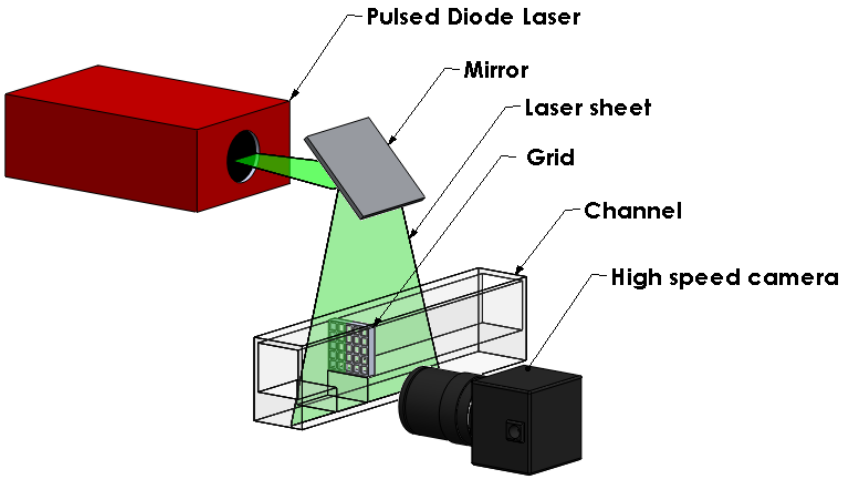

(b)

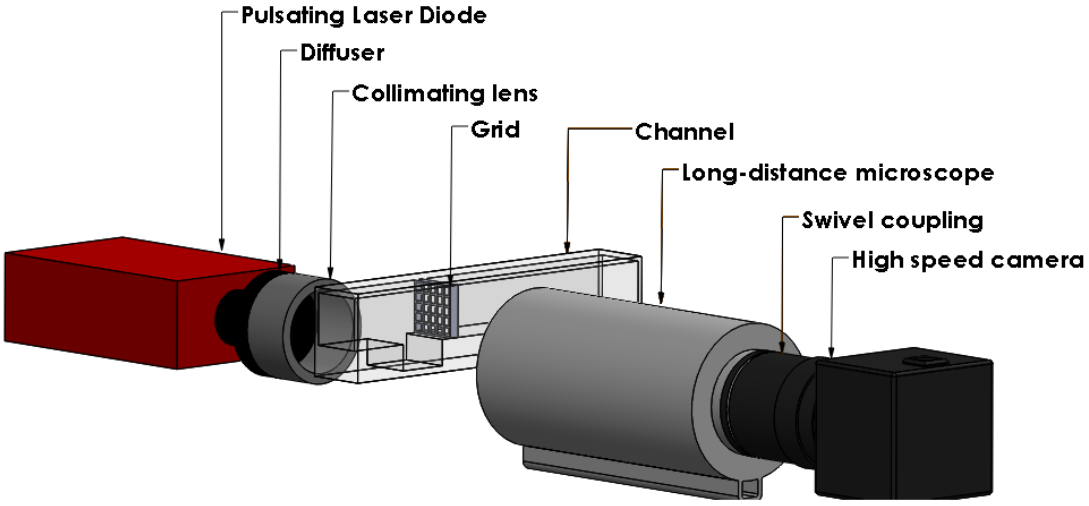

Fig. 2. Schematic layout for PIV (a) and the high-speed, long-distance microscopy (HS-LDM) imaging setup (b)

To investigate the fluidization dynamics of the lactose carrier particles, the centroid, major axis, and minor axis of the carrier particles between two successive frames were calculated using the built-in MATLAB function: region props. The captured particles in each frame are initially sorted based on their x-coordinate location, and captured particles from the first frame are compared to all the captured particles in the second frame. This loop would break when the particle in the first frame of the time sequence was considered the same as the particle in the second frame of the sequence. The captured particles in successive frames were

considered the same if the change in particle size along the minor axis and major axis was less than 12%, and when the particle displacement was less than 60 pixels (0.145 mm) (80 pixels was used for LH200 at 100 L/min for 5 × 5 channel). The velocity of the particles was computed based on their displacement. The particle displacement rejection criterion was adjusted by choosing an appropriate time step between successive frames. Further details to demonstrate the robustness and sensitivity of this rejection criterion are provided in the Appendix. The above process works well for polydisperse mixtures that consist of large isolated carrier particles as is the case here.

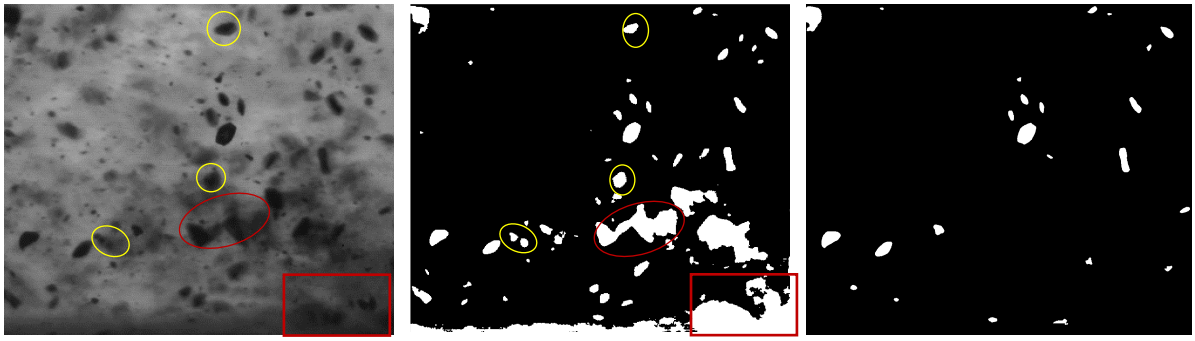

Raw image Binarized image Final image

Fig. 3. Image binarization process

2.3 Powder properties

Four DFE Pharma lactose powders were used in this study, and their properties are listed in table 3. Two powders are milled lactose (LH200 and LH206) from the Lactohale® series while the other two powders are sieved from the Respitose® series. LH200 has the highest percentage of fines compared to other powder, so it has the highest Carr's index (Carr's index % = 39) and lowest flow-ability. SV010 has the largest median diameter (x50 =112 µm), which implies better flow-ability properties (Carr's index % = 17) and less inter-particle force between the particles. SV003 has the smallest median diameter (x50 = 61.6 µm). The powders were loaded into the powder pocket without being packed, and excess powder particles were swept away to ensure that a consistent powder volume was used for all the test cases, following similar procedures published in [16, 24].

Table 3. Key properties of powders used in the experiments where x10, x50 and x90 are the diameter intercepts for 10%, 50% and 90% of the cumulative volume determined from the cumulative particle size distribution, %<Nµm indicates the percentage of fine particles below N µm

	Lactohale® 200	Lactohale® 206	Respitose® SV003	Respitose® SV010
Tapped density (1250 taps) (g/l)	950	720	780	830

Poured density (g/l)	580	870	630	690
Carr's index %	39	17	19	17
x10 (μm)	10.7	32.0	32.3	51.0
x50 (μm)	74.5	84.9	61.6	112.0
x90 (μm)	158.6	166.2	95.7	181.1
Span=(x90-x10)/x50	1.98	1.58	1.03	1.12
%<5 μm	4.8	2.3	2.8	1.6
%<10 μm	16.2	4.1	5.4	3.8
%<15 μm	28.2	6.6	8.6	5.8

The raw images and binarized images obtained using the HS-LDM technique for various powders are presented to provide qualitative information on the local morphology of the powder evacuation process. Images similar to these are used in section 3 onwards to quantify the particle size and velocity. Figs. 4 and 5 show the raw and binarized images of the particles above the powder pocket beside its left edge for powders SV010 and LH200 respectively (The images are taken at the location referred to as "point 1" in Fig. 7(b). Images are darker at the beginning of evacuation because of the dense powder cloud at the start of the process, and the image contrast improves at later time instances. The presence of fine particles is more evident for LH200 compared to SV010, as shown in Fig. 4 given the higher fines percentage in LH200 (%<15 μm =28.2) compared to SV010 (%<15 μm =5.8). A decrease in the flow rate leads to a decrease in the number of particles in the captured frames for no grid cases. For example, the mean number of particles per image for SV010 at point 1 for the 5 × 5 channel was 9.7 particles/image at an air flow rate of 100 L/min compared to 6.94 particles/image at an airflow rate of 40 L/min because of a higher air flow rate which enhances the evacuation of larger powder particles out of the pocket.

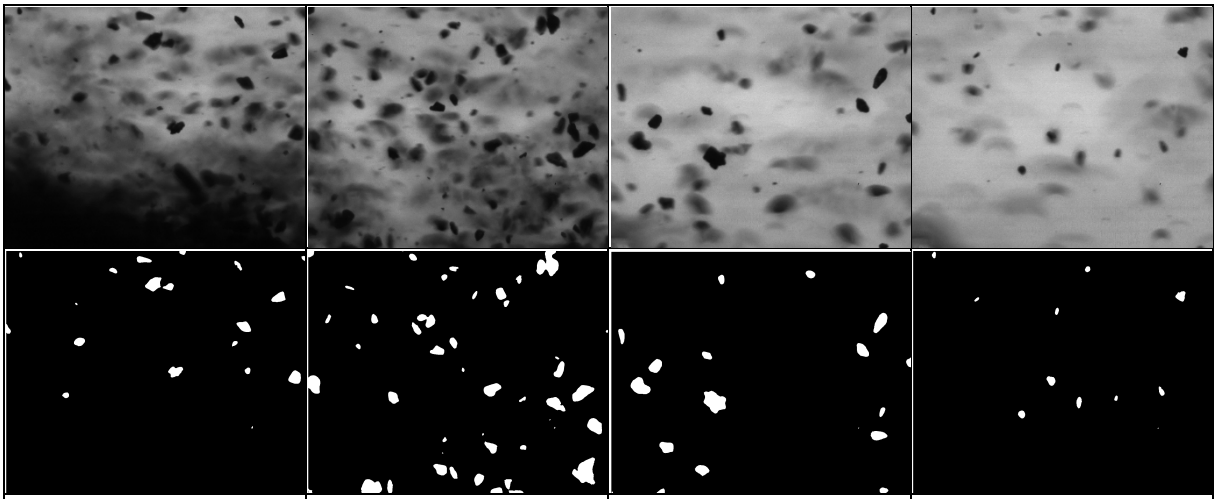

Fig. 4 Representative snapshots for point 1 using SV010 in 10 × 10 channel using a grid with a blockage ratio of ~30 % placed at the pocket edge(x=0mm) at an air flow rate of 80 L/min

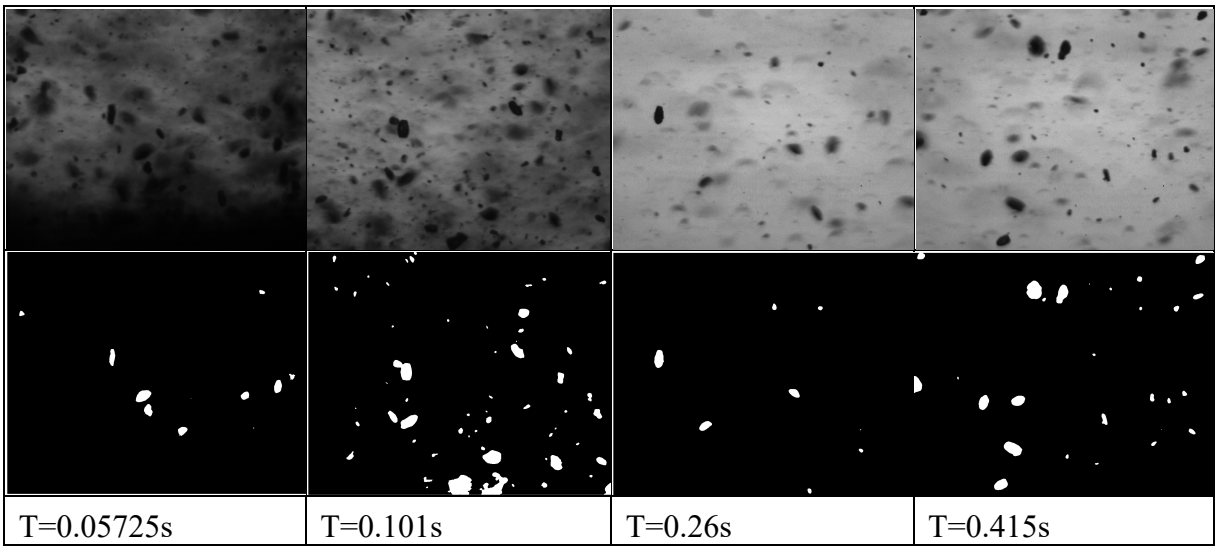

Fig. 5. Representative snapshots for point 1 using LH200 in 10 × 10 channel using a grid with a blockage ratio of ~30 % placed at the pocket edge (x = 0mm) at an air flow rate of 80L/min

3. Results and discussion

The results section will begin by presenting the mean velocity profiles developed in the channel measured using the PIV technique. This will be followed by comparing the mean velocity magnitude at different locations obtained using PIV and HS-LDM. Finally, detailed measurements of the HS-LDM results will be presented to shed light on local particle dynamics conditioned on size.

3.1. Lactose particle velocities obtained using PIV

Figure 6 shows the mean velocity contours and normalized velocity fluctuation of LH200 and SV010 particles on the mid-width plane (10 × 10 channel), using grids with blockage ratio of 25%, 30% and 40%. The powder streamwise turbulence intensity was calculated as the root mean square (RMS) of velocity fluctuations normalized by mean velocity. The measurements are shown at different locations (L) downstream of the powder pocket. As expected, the mean velocity was the highest at the midline of the channel, but the streamline turbulence intensity was the highest along the channel walls due to the local increase in shear. In Fig. 6(a), differences in the development of the velocity profiles along the length of the 10 × 10 channel for LH200 and SV010 at 100 L/min using grids with different blockage ratio can be observed. It is noticed that velocities of the powder particles adjacent to the top wall of the channel are

generally higher compared to the particles at the bottom wall. Larger particles tend to accelerate upwards (away from the bottom wall) due to a vortex-induced in the powder cavity [16, 24] during evacuation and they would subsequently take longer to decelerate due to their inertia.

While a grid's blockage ratio of 25% and 30% do not seem to have a significant effect on the particles' velocities, this is not the case for the grid with a blockage ratio of 40%, where a slight increase in the particles' mean velocities at the powder pocket edge (L=0 mm) can be observed. The mean velocity magnitude of the milled powder (LH200) is larger than the sieved powder (SV010) because the x50 (diameter intercept) for LH200 is smaller than SV010. Fig. 6(b) and Fig. A1(b) show that the streamwise turbulence intensity of LH200 and SV010 decrease as the particles move further away from the grid (as L increases).

The grid with the lowest blockage ratio of 25% has the highest streamwise turbulence intensities at the pocket edge (L=0 mm) compared to the other grids and for all the powders except for SV010. The grid with the highest blockage ratio is also associated with a turbulence intensity profile that varies lesser with distance L, as can be observed in Fig. 6(b), and this is despite the significant decay in mean axial velocity seen in Fig. 6(a).

(a)

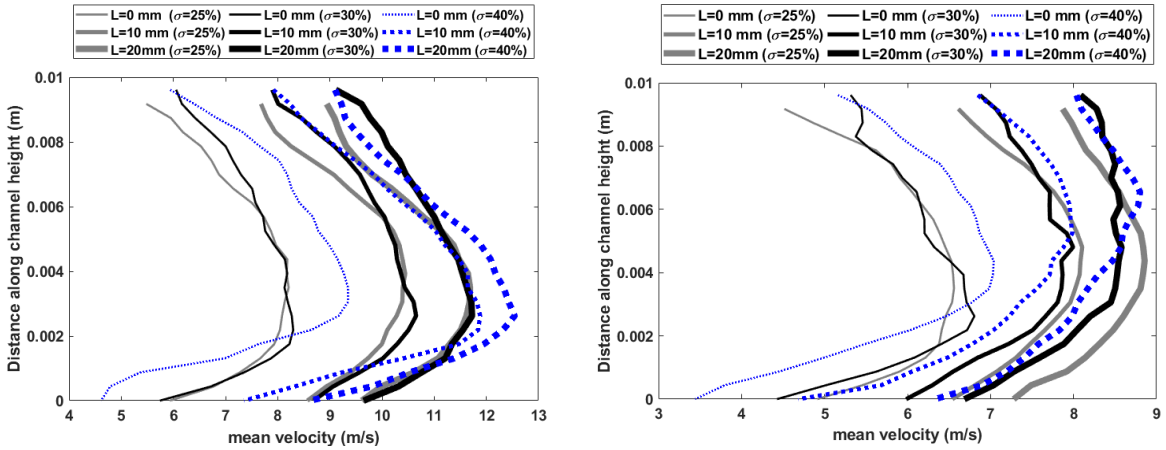

(b)

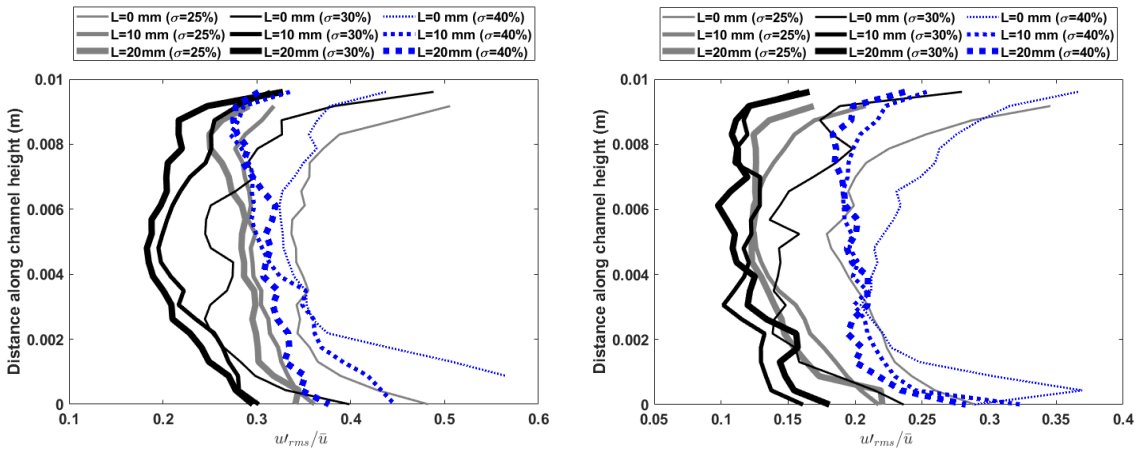

LH200 SV010

Fig. 6. General flow characteristics using grids with different blockage ratio (σ) placed at the pocket edge (x=0 mm) at 100 L/min: (a) mean velocity profiles, and (b) streamwise turbulence intensity.

3.2. Comparison of measurements produced by PIV and HS-LDM

Both PIV and HS-LDM were used to analyze the mean particle velocities at specific locations in the channel. For the no-grid cases, three locations were chosen in the 5 × 5 and 10 × 10 channel, and they are shown in Fig. 7(a). For the grid cases, five locations were chosen in the 10 × 10 channel (see Fig.7(b)). The locations of points 3, 4, and 5 were 10 mm away from the powder pocket edge.

It can be observed from Fig. 8 that both the PIV and HS-LDM produced very similar results at different locations selected in the 5 × 5 channel. The mean velocity magnitude of SV010 measured using the two different techniques is similar, particularly at points 2 and 3. In a more dispersed flow where the grid with blockage ratio of 30% was placed before the powder pocket at (x = 0mm) in the 10 × 10 channel, the results from the two techniques still follow the same trend as shown in Fig 9. The above shows that the rejection criteria set from the (HS-LDM) images as described in section 2.1 are appropriate, given the comparison with PIV, which is a planar measurement.

Velocity magnitude increases with distance away from the pocket, and this is due to the acceleration of the particles. The velocity in Point 5 in the 10 × 10 channel with the grid is lower compared to point 4, and this can be explained by the tendency of larger particles to travel upwards which is evident in Fig. 10. As described earlier, a vortex developed in the pocket corner, and this affected the velocity of all particle sizes. However, due to the inertia of larger particles, they did not follow the mean flow stream (from right to left) immediately as they left the powder pocket, but followed a slightly angled vertical trajectory which was a combination of the "memory" of the local vertical velocity from the pocket (which ejects powder upwards due to recirculation) and the subsequent mean flow. This is in contrast to non-inertial smaller powder particles, that simply followed the mean flow stream the moment they vacated the pocket. The above demonstrates a complex interaction between local particle size and velocity that can develop even in a basic geometry, information of which could not be obtained without locally measuring both size and velocity, which highlights the usefulness of the HS-LDM technique.

From Fig 8, it can also be seen that the mean velocity magnitude increases with an increase in the air flow rate. The LH200 powder has the highest mean velocity magnitude at the three different points and for different flow rates due to the highest percentage of fines (%<15 μm = 28.2), which tends to travel at a higher speed (lower inertia). LH200 and SV003

tend to have quite similar mean velocity magnitudes in most of the cases especially at air flow rates of 80, 60, and 40 L/min because the x50 for SV003 is quite close to the x50 for LH206 (x50 for SV003 = 61.6 µm, x50 for LH206 = 84.9 µm). SV010 has the slowest particle velocities for the tested flow rates as it has the largest median diameter (x50 = 112 µm). The reader should note that previous work [19] has demonstrated that the evacuation of SV010 from the powder pocket was more rapid compared to other powders due to lower cohesion (associated with a smaller fine particle fraction compared to LH200). The results here demonstrate that despite a faster evacuation (which is due to lower bulk cohesion), individual SV010 particles travel at a slower speed due to their larger particle size for subsequent evacuation from the pocket.

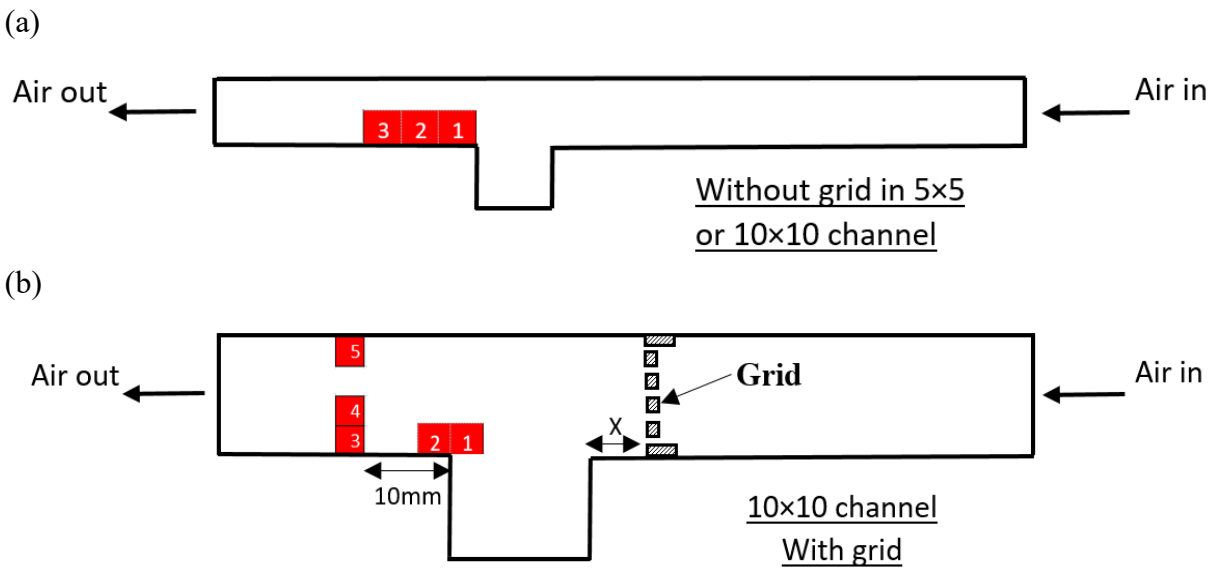

Fig. 7: Location of the points at which velocity was calculated: (a) no grid case in 5 × 5 or 10× 10 channel, and (b) grid case in 10 × 10 channel.

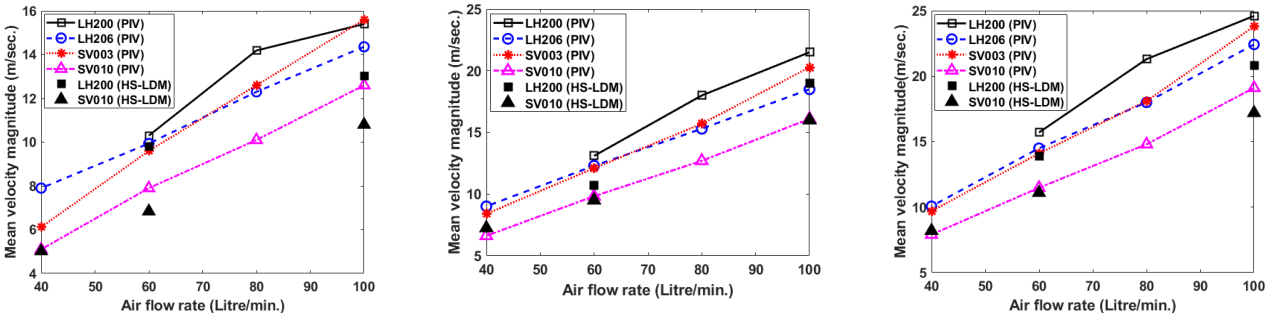

Point 1 Point 2 Point 3

Fig. 8. Mean velocity magnitude using PIV and HS-LDM techniques in 5 × 5 channel for different locations: (a) point 1, (b) point 2, and (c)point 3

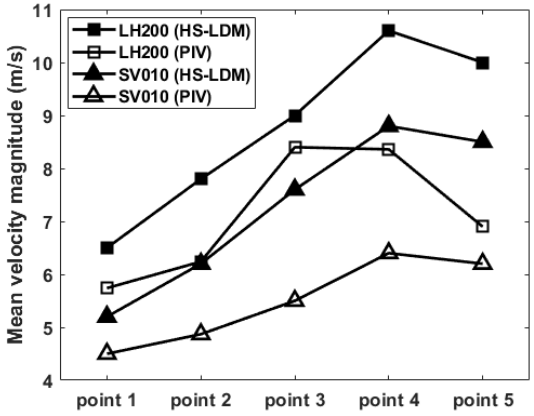

Fig. 9. Comparison between results obtained from PIV and HS-LDM techniques in 10 × 10 channel at an air flow rate of 80 L/min using a grid with blockage ratio of 30% placed at the pocket right edge(x=0mm) for different locations

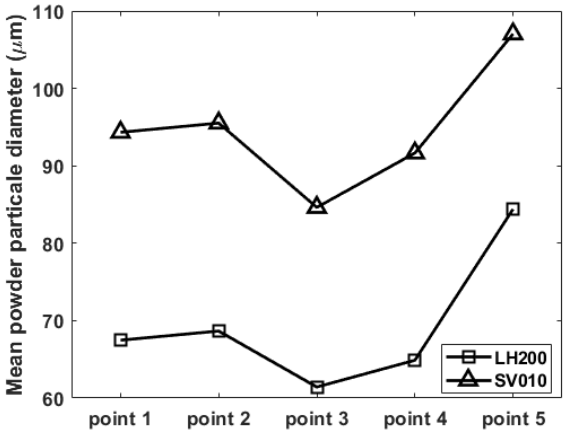

Fig. 10. Mean powder particles diameter for LH200 and SV010 in 10 × 10 channel using a grid with a blockage ratio of ~30 % placed at the pocket edge(x=0mm) at an air flow rate of 80 L/min using HS-LDM technique

Further detailed insights on the local powder flow-field can be obtained through observation of the statistical distribution of velocity for different powders and flowrates. Fig. 11 shows the probability distributions for different flowrates and powders just after the powder pocket (point 1) using PIV. This data is produced by examining a single interrogation window adjacent to the pocket and building a probability distribution over time. The results demonstrate that the mode (the most frequent value in the data set) of the velocity distribution for different powders is quite similar at a high flow rate of 100 L/min for the 5 × 5 channel which corresponds to an air flow Reynolds number of 22,560. In contrast, for a lower flow rate of 60 L/min, it can be seen that the mode of the sieved lactose powder tends to shift in a different direction, in which SV010 has the smallest mode, and SV003 tends to have the highest distribution mode which agrees with the mode shapes of the volume-based particle size distribution (PSD) density shown in Fig.12. This shows that the powder properties are more dominant at a low flow rate which agrees with previous work [19] and also demonstrates that the local probability of a particular velocity band being measured is linked to the particle size distribution of the powder.

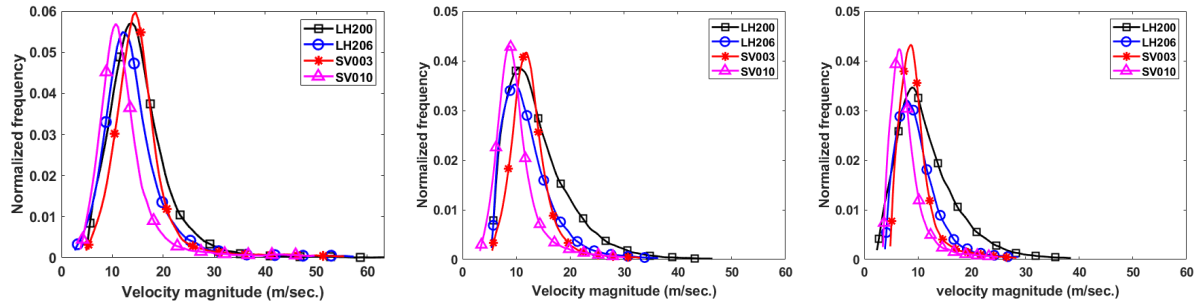

100 L/min 80 L/min 60 L/min

Fig. 11. Velocity magnitude distribution for point 1 in 5 × 5 channel for different flow rate and powder using PIV technique

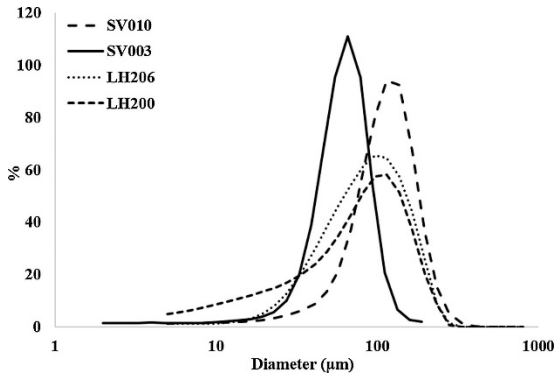

Fig.12. Volume-based particle size distribution (PSD) density of various powders tested (DFE Pharma). (Note: Permission will be obtained from publisher prior to publication)

3.3. Sub-ranged powder particle dynamics

All previous sections have examined local velocity characteristics by averaging all particle size bands. This is not only important to provide a global picture of the local flow-field and the effect of powder properties and flowrate but was also necessary to compare the PIV and HS-LDM techniques.

In this section, the powder particle dynamics will be investigated by using the particle tracking data from the HS-LDM measurements. The above will enable understanding of how the polydisperse nature of the powder particles affects the dynamics of the powder. As mentioned, the key advantage is that the technique has the advantage of providing information of the powder particle dynamics conditioned on particle size and this information is useful to improve understanding of the role of fine carrier particles which is fundamental to improve DPI performances.

Fig.13 presents the streamwise RMS of velocity fluctuations of powder particles conditioned (or "sub-ranged") on different sizes which are obtained by measuring the local velocity for different equivalent diameters. The key aim of this section is to examine how different particle sizes respond to the surrounding flow-field, and this is achieved by measuring the local RMS of velocity fluctuation for each particle size band and normalizing it by the locally measured gas-phase RMS fluctuating velocity. This data is then plotted against both the particle mean diameter (D_n) and Stokes number (St).

The equivalent diameter was calculated by measuring the minor and major axes of the powder particles from the HS-LPM images. Powder particle size bands ranging from 0–25, 25–50, 50–100, 100–150 and 150–250 μm were used. The first sub-range of powder particles represents the gas phase. Calculation of the Stokes numbers confirms that the smallest size band chosen reasonably represents the gas phase.

The Stokes number is defined as St=τ_d/τ_t where τ_d is the relaxation time of the particle and τ_t are the flow timescale given in Eqs. (1) and (4) respectively, where subscripts *g* and *p* refer to gas and particle phases, respectively. The drag coefficient C_d and the particle Reynolds number Re_p are defined in Eqs. (2) and (3). The turbulence length scale Λ is the mesh size for grid cases [25], and 5% of the channel height for the no grid cases [24]. $|U_s|$ is the absolute value of the mean slip velocity of particular particle size (*d)* with respect to the gas phase and u' is the gas phase RMS fluctuating velocity.

It can be observed from Fig.13 that the particle RMS fluctuating velocity decreases with the increase in the particle mean diameter(D_n) for the different point locations specified in Fig. 7. Moreover, the RMS fluctuating velocity for points 4 and point 5 are slightly higher compared to the other points as shown for LH200 and SV010 as shown in Figs 13(a) and (b) respectively.

Interestingly, when U'_{D_n}/U'_{gas} is plotted against the Stokes number (St) for the different point locations (defined in Fig.7), the curves collapse over each other for LH200 and SV010 as shown in Fig 13(c) and (d) respectively. This may be explained by the larger turbulence time scale (τ_t) for point locations 4 and 5 because of a lower gas-phase fluctuating velocity (u'), which leads to those two points having a lower Stokes number, hence shifting curves for the point locations 4 and 5 to be on top of point locations 1 and 3 in Fig. 13(c) (when compared to Fig. 13(b)). Moreover points 4 and 5 have a larger particle diameter in the first size band resulting in lower u'_{gas}. This is an interesting result as it demonstrates that even though the two powders (LH200 and SV010) have very different fine particle fraction, and measurements are taken in two different locations in the channel flow, the use of a local dimensionless scale, allows all of the data to be more "universally" described.

For the 5 × 5 channel in which no grid was used, (U'_{D_n}/U'_{gas}) was plotted against Stokes number, as shown in Fig. 14 for different flow rates and powders. It can be seen that an increase in air flow rate leads to an increase in (U'_{D_n}/U'_{gas}) for all cases in Fig. 14 except for LH200 at point location 3. Moreover, SV010 tends to have higher (U'_{D_n}/U'_{gas}) compared to LH200 at 100 L/min. In addition, stokes number increases with the increase of air flow rate because of the decrease in the flow timescale (τ_t) induced by the increase of gas fluctuating velocity (U'_{gas}). The reader should note that the "collapse" of data with Stokes number shown in Fig. 13 occurred only when moving spatially in the channel but clearly does not occur with an increase in the global flowrate. This is most likely due to the significant change in the magnitude of the fluctuating velocity with flowrate, which impacts both on the local Stokes number value and turbulence intensity. Further work is merited to develop correlations between flowrate and Stokes number for this particular configuration; however, this is beyond the scope of this study.

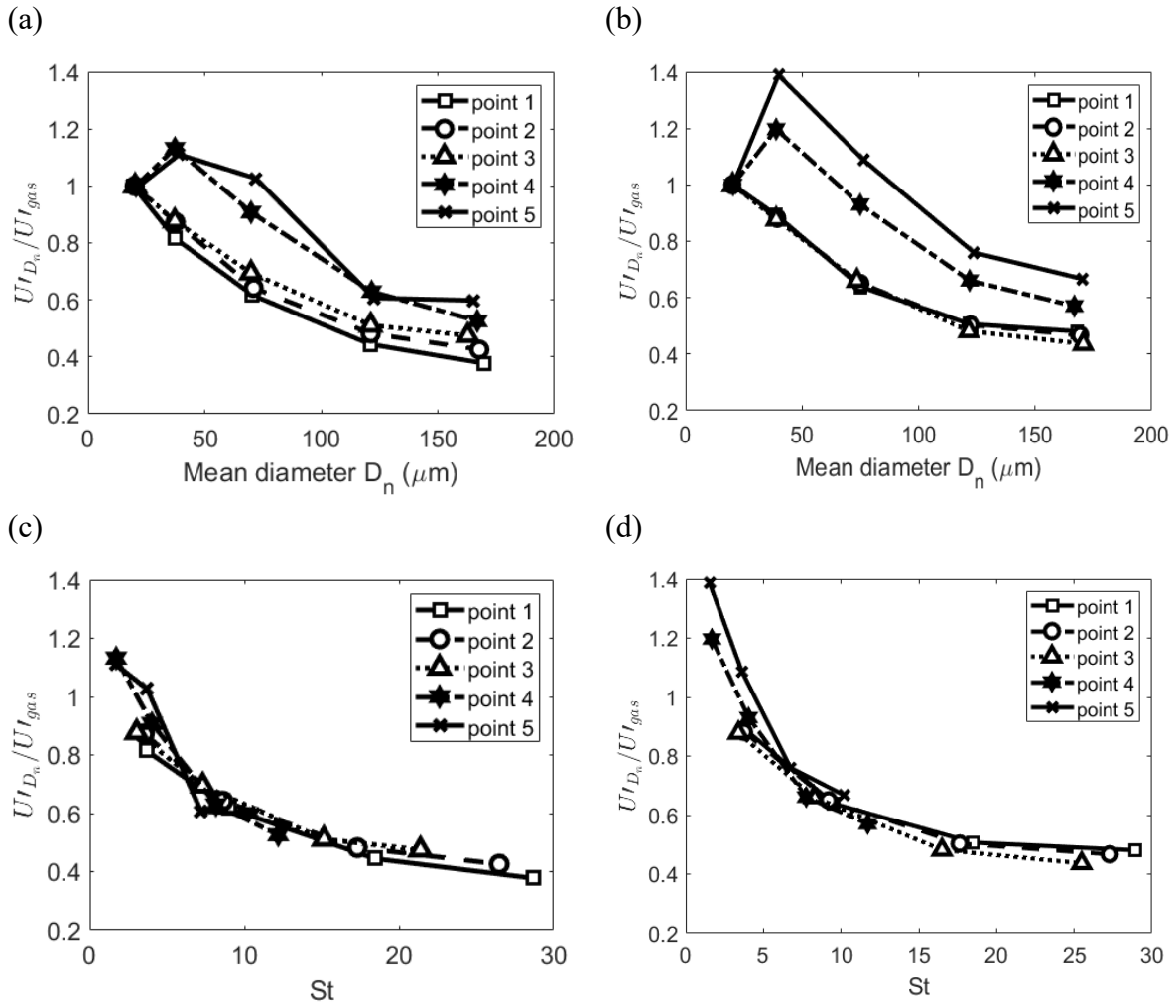

Fig. 13. RMS fluctuation of streamwise velocity (U'_{D_n}) normalized by RMS fluctuation of the gas phase axial velocity U'_{gas} for different points at an air flow of 80 L/min using a grid with a blockage ratio of 30% *for 10 × 10 channel: (a) versus mean diameter (D_n) for LH200, (b) versus mean diameter (D_n) for SV010, (c) versus stokes number (St) for LH200, and (d) versus stokes number (St) for SV010*

(a) (b)

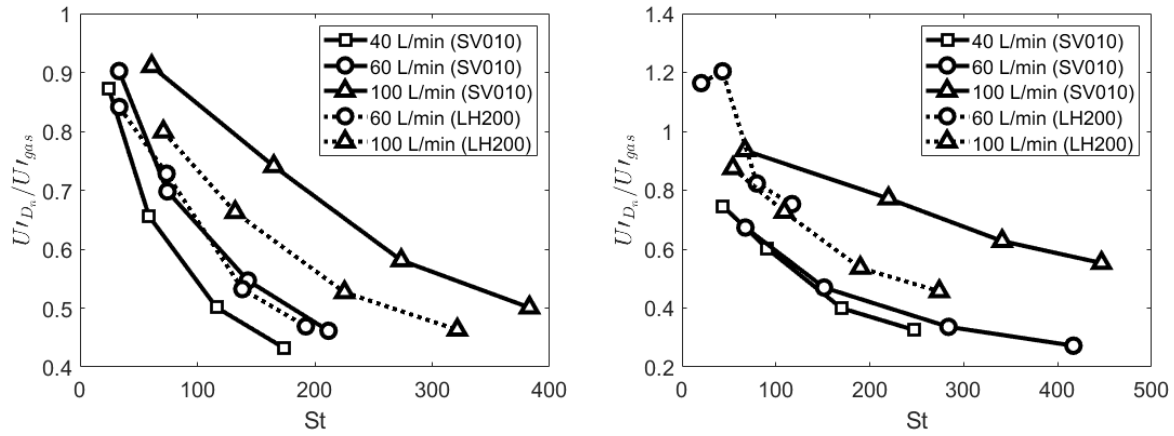

Point 1 Point 3

Fig. 14. RMS fluctuation of streamwise velocity (U'_{D_n}) normalized by RMS fluctuation of the gas axial velocity (U'_{gas}) in 5 × 5 channel for different point locations: (a) point location 1 ,and (b) point location 2

$$\tau_d = \frac{4}{3}\frac{\rho_p}{\rho_g}\frac{d}{C_d\,|U_s|} \quad (1)$$

$$C_d = \frac{24}{Re_p}\left(1 + 0.15\,{Re_p}^{0.687}\right) \quad (2)$$

$$Re_p = \frac{d\,U_s}{\upsilon_{gas}} \quad (3)$$

$$\tau_t = \frac{\Lambda}{u'} \quad (4)$$

Further insights can be obtained using the local fluctuation data by examining the propensity for the powder to deviate from the mean flow. The term $(\mathrm{v}'/\mathrm{U})_{D_n}$, or the spanwise RMS fluctuations normalized by the mean axial velocity can be used as a measure for how much particle deviation occurs away from the main flow direction [26]. This is plotted for different particle size bands, as shown in Fig. 15. It can be observed that the measurements at point locations 1 and 2 have higher values compared to point locations 3 and 4. As points 1 and 2 are close to the powder pocket, which is indicative of the main area where particles are initially emerging out of the pocket, they are more likely to spread across the channel subsequently. The data shows that at point locations 3 and 4, which are located 10 mm away from the powder pocket edge, powder particles tend to follow the horizontal direction of the main flow more effectively as they are exhibited to less spanwise fluctuation. Point location 5 has an increasing trend of the term $(\mathrm{v}'/\mathrm{U})_{D_n}$ with the increase of the powder particle size bands. The result once again infers that larger powder particles at point 5 tend to move upward

compared to smaller powder particles, due to maintaining inertia from the initial vortex that formed in the powder pocket.

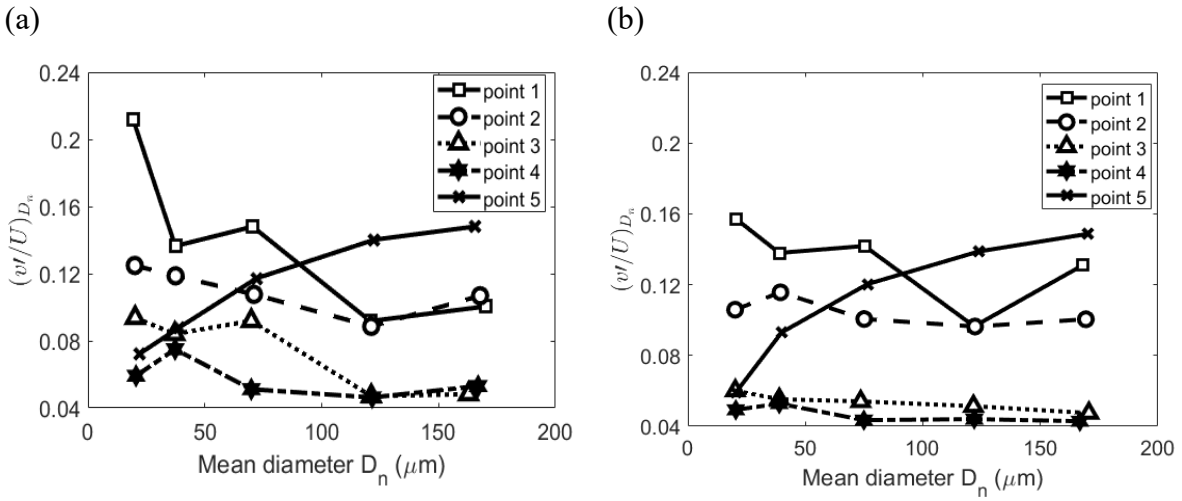

Fig. 15. $(v'/U)_{D_n}$ *versus mean particles diameter for: (a)LH200, and (b) SV010*

4. Conclusions

High-speed, Long-distance microscopy (HS-LDM) enables high-resolution characterization of pharmaceutical powder particle morphology and time-resolved dynamics. This paper has explored the use of the above technique in a pharmaceutical powder fluidization problem and compared it to PIV. Information about powder particle velocities according to size can be used towards obtaining a better understanding of the role of carrier particles on the performance of a DPI like device. The key conclusions of the paper are as follows:

- The measurements show that powder particle velocities are affected by the fines percentage and the median diameter. Powders with high fines percentages tend to have a higher mean velocity and particles with larger median diameter tend to travel at a slower speed.
- The use of a grid increased the local powder particle velocities, promoted the dispersion of particles, and enabled a direct comparison between PIV and high-speed, long distance microscopic (HS-LDM) imaging. This study confirms that the HS-LDM technique can capture the overall mean velocity adequately.
- The span of velocity closely follows that of the particle size distribution both for cohesive and non-cohesive powders.
- The response of particles to the surrounding carrier flow (measured through their RMS of velocity fluctuations with respect to fluctuations of the gas phase) demonstrated that the trend of size conditioned fluctuations with Stokes numbers is not particularly sensitive to the location in the turbulent channel flow.

Acknowledgements

Funding for the research was made possible, in part, by the Australian Research Council through grant DP190101237 and the Food & Drug Administration (United States) through grant 1U01FD006525-01. Views expressed do not necessarily reflect the official policies of the Department of Health and Human Services; nor does any mention of trade names, commercial practices, or organization, imply endorsement by the United States Government. The first author is funded by a PhD scholarship from the Australian Government Research Training Program.

Appendix

1- General flow field

Mean velocity profiles and streamwise turbulence intensities for the other two powder used in this study (LH206, and SV003)

(a)

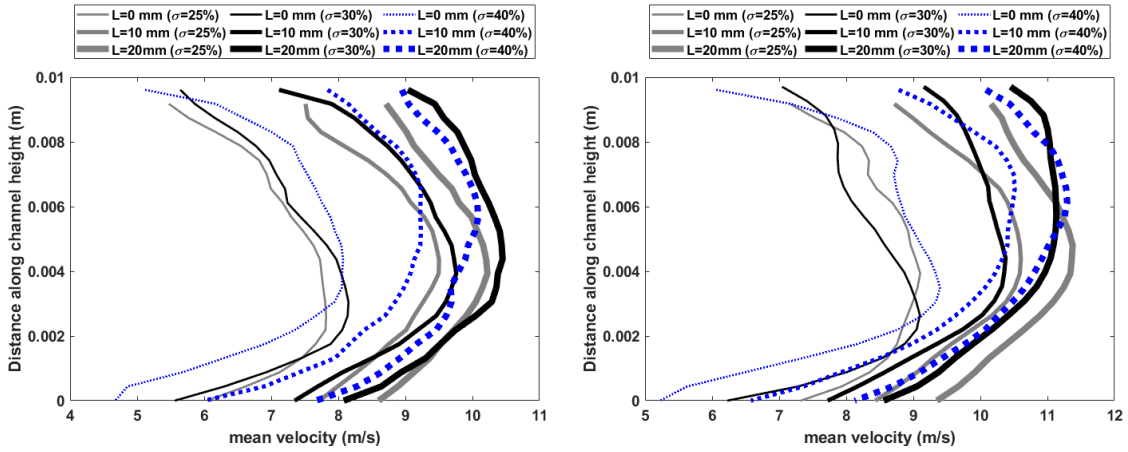

(b)

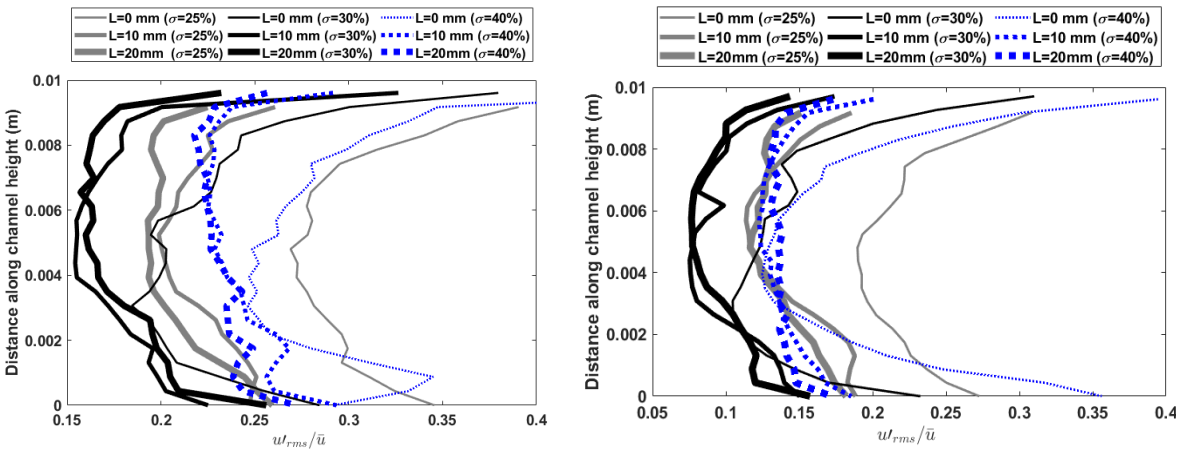

LH206 SV003

Fig.A1. General flow characteristics using grids placed at the pocket edge (x=0mm) at 100 L/min: (a) mean velocity profiles, and (b) streamwise turbulence intensity

2- Powder particle mean diameter measurement

Mean equivalent diameter for the powder particles was calculated for a different location in the 5 × 5 channel. The equivalent diameter was calculated for each particle using major and minor axes length. It can be seen that the mean diameter for LH200 is smaller compared to SV010, which agree with the x50 trends for LH200 (x50=74.5µm) and SV010(x50=112 µm).

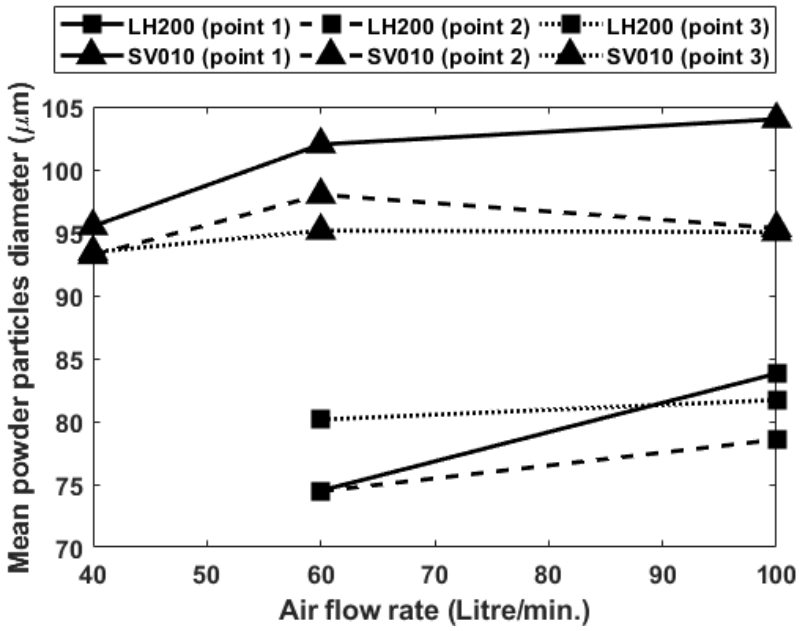

Fig. A2. Mean powder particles diameter for LH200 and SV010 in 5 × 5 channel for different air flow rates using a high-speed, long-distance microscopy (HS-LDM) technique

3-$(v'/U)_{D_n}$ for LH200 and SV010

Different trials for figure 17 plotted in red lines to make sure that the observed trend for that term $(v'/U)_{D_n}$ is consistent.

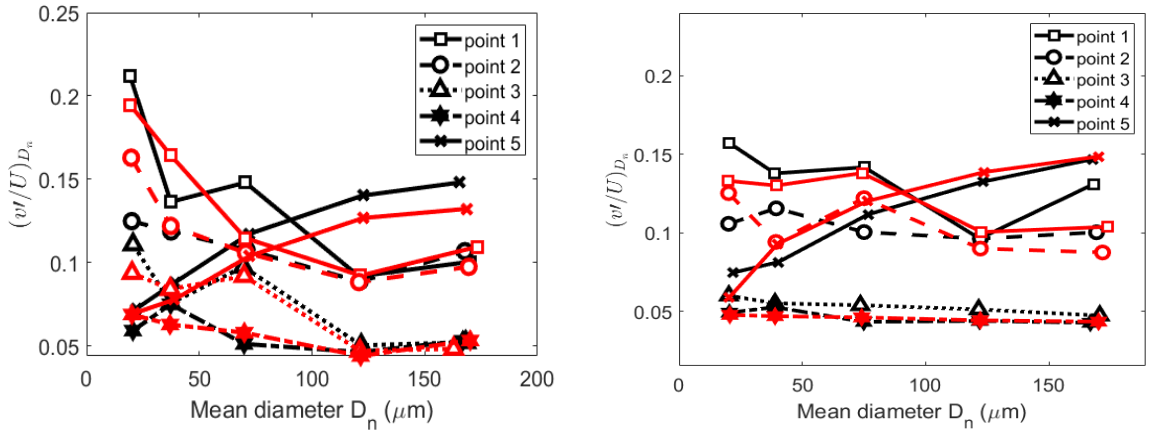

*red lines refer to other trials

Fig. A3. $(v'/U)_{D_n}$ *versus mean particles diameter in 10 × 10 channel for: (a)LH200, and (b) SV010*

4- Studying the effect of changing PIV final interrogation window size

Table A1: Mean u and v for all point at the mean flow field for 5 × 5 channel without grid at 100 L/min using SV010

5 × 5 channel without grid at 100 L/min using SV010				
No of pass/final pass size	U (m/s)		V(m/s)	
	mean	std	mean	std
1 pass/ 64 × 64	21.64	4.4967	1.577	0.976
2 pass/ 32 ×3 2	22.53	5.05	1.45	0.78
3 pass /16 × 16	20.01	4.0	1.32	0.503

Table A2: Mean u and v for all point at the mean flow field for 10 × 10 with a grid at 80 L/min using SV010

10 × 10 with a grid at 80 L/min using SV010				
No of pass/final pass size	u(m/s)		v(m/s)	
	mean	std	mean	std
1 pass/ 64 × 64	5.543	1.58	0.411	0.366
2 pass/ 32 × 32	5.581	1.637	0.429	0.411
3 pass /16 × 16	5.58	1.29	0.426	0.39

5- PIV Convergence study

Mean stand deviation of velocity were calculated using the first 500 images for the points located along the same vertical axis, then for the first 1000 image till the whole frames are included, then residual is calculated by subtracting the mean of each set from the mean of the previous set of images. Mean residual along the vertical line is calculated for different locations (L).

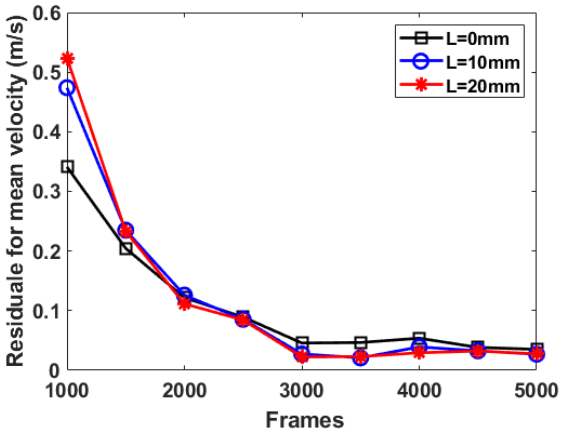

(a) SV010 at 100 L/min using grid with blockage ratio of 30% (x=0mm) for 10 × 10 channel

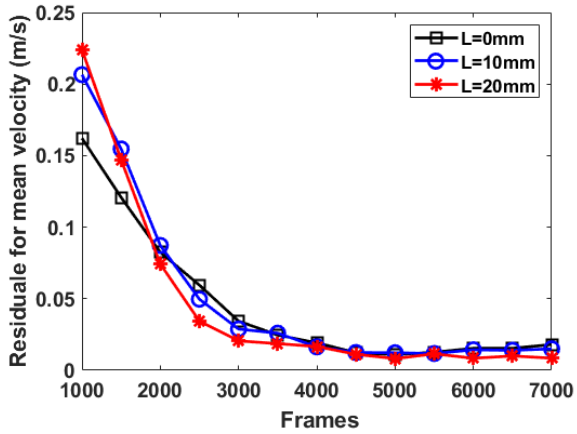

(b) SV010 at 40 L/min using grid with blockage ratio of 30% (x=0mm) for 10 × 10 channel

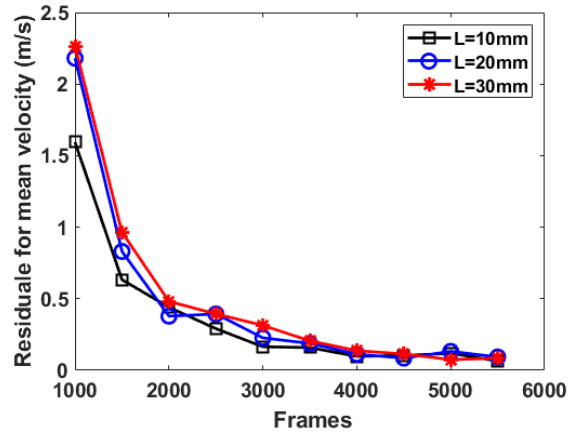

(c) SV010 at 100 L/min for 5 × 5 channel

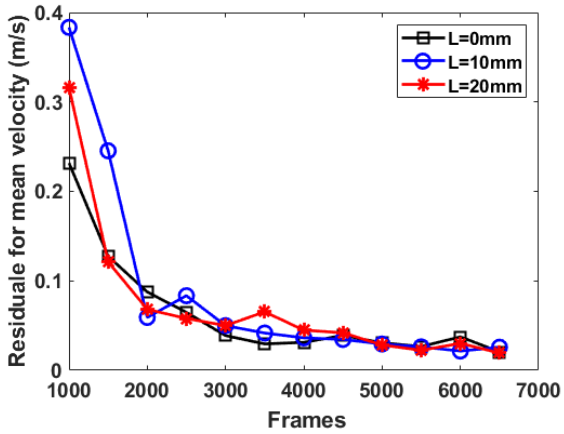

(d) SV010 at 40 L/min for 5 × 5 channel

Fig. A4. PIV convergence study for the mean velocity for different cases

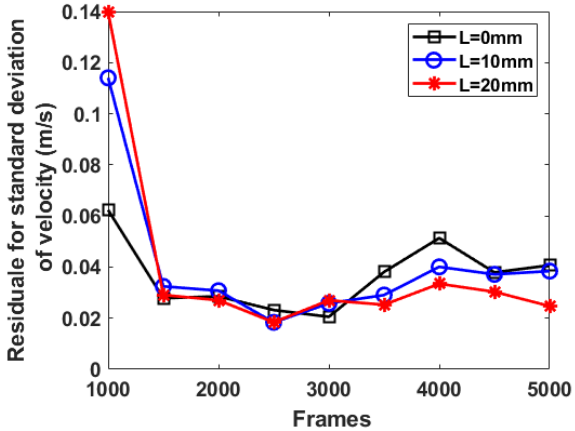

(a) SV010 at 100 L/min using grid with blockage ratio of 30% (x=0mm) for 10 × 10 channel

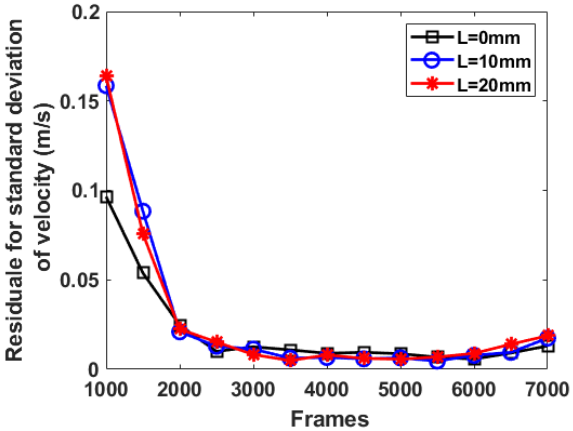

(b)SV010 at 40 L/min using grid with blockage ratio of 30% (x=0mm) for 10 × 10 channel

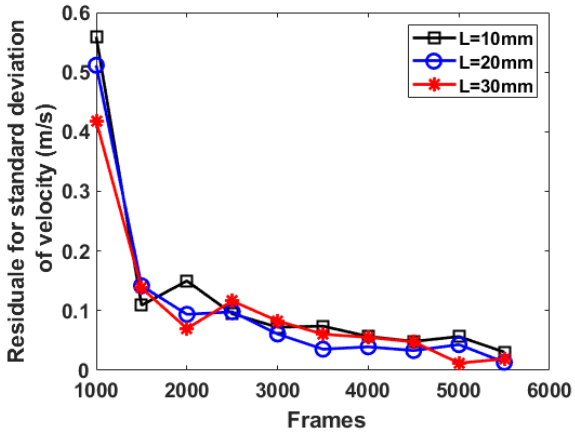

(c) SV010 at 100 L/min for 5 × 5 channel

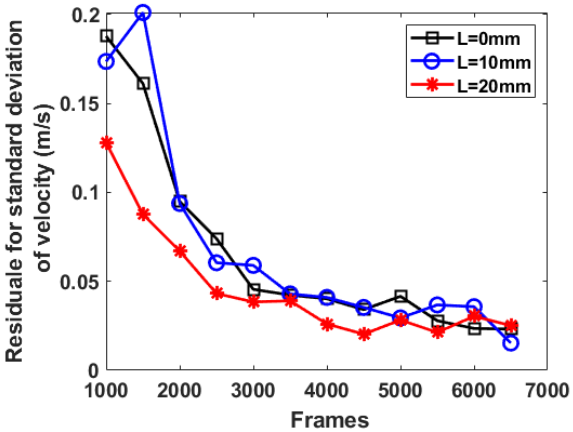

(d) SV010 at 40 L/min for 5 × 5 channel

Fig. A5. PIV convergence study for the standard deviation of the velocity for different cases

6-Sensitivity analysis for the rejection criteria for High-speed, long-distance microscopy (HS-LDM)

6.1- Minor and major diameter rejection criteria

Table A3: Point 4 using SV010 at 80 L/min using a grid in 10 × 10 channel

Percentage	Mean velocity (m/s)	Mean diameter (µm)	Number of particles
5%	8.652	98.78	5264
8%	8.76	95	6136
12%	8.81	92.9	6608
16%	8.843	91.56	6885
20%	8.846	90.9	7033

Table A4: Point 3 using SV010 at 100 L/min using a grid in 5 × 5 channel

Percentage	Mean velocity (m/s)	Mean diameter (µm)	Number of particles
5%	16.83	103.94	4393
8%	17.046	98.94	5817
12%	17.24	95.03	6852
16%	17.33	93.0264	7407

6.2- Maximum particles displacement rejection criteria

Table A5: Point 4 using SV010 at 80 L/min using grid in 10 × 10 channel

Displacement (pixel)	Mean velocity (m/s)	Mean diameter (µm)	Number of particles
40	8.49	97.13	6167
50	8.79	93.15	6585
60	8.81	92.9	6608
70	8.8153	92.9	6608
80	8.818	92.915	6609

Table A6: Point 3 using SV010 at 100 L/min using grid in 5 × 5 channel

Displacement (pixel)	Mean velocity (m/s)	Mean diameter (µm)	Number of particles
40	14.89	103.113	4767
60	17.24	95.03	6852
80	17.55	93.94	6995
100	17.6	93.9	7000

Table A6: Point 3 using LH200 at 100 L/min using grid in 5 × 5 channel

Displacement (pixel)	Mean velocity (m/s)	Mean diameter (µm)	Number of particles
60	19.84	85.49	3928
80	20.92	81.92	4298
100	21.0	81.84	4307

References

1. Peng, T., et al., *Influence of physical properties of carrier on the performance of dry powder inhalers.* Acta pharmaceutica sinica B, 2016. 6(4): p. 308-318.
2. Frijlink, H. and A. De Boer, *Dry powder inhalers for pulmonary drug delivery.* Expert opinion on drug delivery, 2004. 1(1): p. 67-86.
3. Chew, N.Y. and H.-K. Chan, *Influence of particle size, air flow, and inhaler device on the dispersion of mannitol powders as aerosols.* Pharmaceutical Research, 1999. 16(7): p. 1098-1103.
4. Chan, H.-K., *Dry powder aerosol delivery systems: current and future research directions.* Journal of aerosol medicine, 2006. 19(1): p. 21-27.
5. de Boer, A.H., H. Chan, and R. Price, *A critical view on lactose-based drug formulation and device studies for dry powder inhalation: which are relevant and what interactions to expect?* Advanced drug delivery reviews, 2012. 64(3): p. 257-274.
6. Yang, M.Y., J.G.Y. Chan, and H.-K. Chan, *Pulmonary drug delivery by powder aerosols.* Journal of controlled release, 2014. 193: p. 228-240.
7. Kaialy, W., et al., *Effect of carrier particle shape on dry powder inhaler performance.* International journal of pharmaceutics, 2011. 421(1): p. 12-23.
8. Guenette, E., et al., *Understanding the effect of lactose particle size on the properties of DPI formulations using experimental design.* International journal of pharmaceutics, 2009. 380(1-2): p. 80-88.
9. Zhou, Q.T., et al., *Understanding the influence of powder flowability, fluidization and deagglomeration characteristics on the aerosolization of pharmaceutical model powders.* European Journal of Pharmaceutical Sciences, 2010. 40(5): p. 412-421.
10. Shur, J., et al., *The role of fines in the modification of the fluidization and dispersion mechanism within dry powder inhaler formulations.* Pharmaceutical research, 2008. 25(7): p. 1631-1640.
11. Han, R., G. Papadopoulos, and B. Greenspan, *Investigation of powder dispersion inside a SPIROS® dry powder inhaler using particle image velocimetry.* Powder technology, 2002. 125(2-3): p. 266-278.
12. Han, R., G. Papadopoulos, and B.J. Greenspan, *Flow field measurement inside the mouthpiece of the Spiros inhaler using particle image velocimetry.* Aerosol Science & Technology, 2002. 36(3): p. 329-341.
13. Kou, X., et al., *Powder dispersion mechanisms within a dry powder inhaler using microscale particle image velocimetry.* International journal of pharmaceutics, 2016. 514(2): p. 445-455.
14. Pasquali, I., et al., *Optical diagnostics study of air flow and powder zfluidization in Nexthaler®—Part I: Studies with lactose placebo formulation.* International journal of pharmaceutics, 2015. 496(2): p. 780-791.
15. Ngoc, N.T.Q., et al., *Experimental investigation of design parameters on dry powder inhaler performance.* International journal of pharmaceutics, 2013. 457(1): p. 92-100.
16. Tuley, R., et al., *Experimental observations of dry powder inhaler dose fluidization.* International journal of pharmaceutics, 2008. 358(1-2): p. 238-247.
17. Versteeg, H.K. and R.D. Wildman. *An optical method for the study of aerosol generation in dy powder inhalers*. in *ASME 7th Biennial Conference on Engineering Systems Design and Analysis*. 2004. American Society of Mechanical Engineers.
18. Voss, A. and W.H. Finlay, *Deagglomeration of dry powder pharmaceutical aerosols.* International journal of pharmaceutics, 2002. 248(1-2): p. 39-50.
19. Elserfy, K., et al., *Effect of an upstream grid on the fluidization of pharmaceutical carrier powders.* International Journal of Pharmaceutics, 2020. 578: p. 119079.
20. Kourmatzis, A., P.X. Pham, and A.R. Masri, *A two-angle far-field microscope imaging technique for spray flows.* Measurement Science and Technology, 2017. 28(3): p. 035302.

21. Kourmatzis, A., P.X. Pham, and A.R. Masri, *Characterization of atomization and combustion in moderately dense turbulent spray flames.* Combustion and Flame, 2015. 162(4): p. 978-996.
22. Lowe, A., A. Kourmatzis, and A.R. Masri, *Turbulent spray flames of intermediate density: Stability and near-field structure.* Combustion and Flame, 2017. 176: p. 511-520.
23. Thielicke, W. and E. Stamhuis, *PIVlab–towards user-friendly, affordable and accurate digital particle image velocimetry in MATLAB.* Journal of Open Research Software, 2014. 2(1).
24. Mahmoudi, S., et al., *Fluidisation characteristics of lactose powders in simple turbulent channel flows.* Experimental Thermal and Fluid Science, 2019. 103: p. 201-213.
25. Pope, S.B., *Turbulent flows*. 2001, IOP Publishing.
26. Kourmatzis, A., W. O'Loughlin, and A. Masri, *Effects of turbulence, evaporation and heat release on the dispersion of droplets in dilute spray jets and flames.* Flow, turbulence and combustion, 2013. 91(2): p. 405-427.